Monte Carlo simulations for $e^+e^- \to n\,\overline{n}\,\gamma_{\rm IS}$ at BESIII

Abstract: We study Monte Carlo simulations for processes $e^+e^- \to n\,\overline{n}\,\gamma_{\rm IS}$ at BESIII to estimate the energy resolution.

Contents

1. Reconstruction of $n\overline{n}$ center of mass energy E_{nn}

A $n\,\overline{n}\,\gamma_{\rm IS}$ final state is generated with the initial state (IS) photon $\gamma_{\rm IS}$ emitted at zero degrees. The 4-momenta uncertainties have been included in this way:

- for the IS photon we consider

$$\delta E_{\gamma_{\rm IS}} = C_0 + \frac{C_1}{\sqrt{E_{\gamma_{\rm IS}}/\mathrm{GeV}}}\,, \tag{1.1}$$

with constants C_0 and C_1

Material	C_0	C_1
LYSO	2.65%	1.81%
W-Scint	3.67%	7.37%

. (1.2)

- For what concerns the anti-neutron, we assume as uncertainty in momentum the error due to the TOF resolution which is $\delta t = 150$ ps. In order to propagate such an error on the modulus of the anti-neutron 3-momentum and its scattering angle, we consider the two possible cases that can occur if the anti-neutron hits the detector:
  - if the scattering angle is $35^o \leq \theta_1 \leq 145^o$ then the anti-neutron ends up in the barrel and, following the scheme given in fig. **??** (consider the shorter red trace), the time-of-flight is

$$\begin{aligned} t_1 &= \frac{R}{\sqrt{v_x^2+v_y^2}} = \frac{E\,R}{c^2\sqrt{p_x^2+p_y^2}} = \frac{E\,R}{c^2|\vec{p}\,|\sin\theta_1} = \frac{R\,c\sqrt{\vec{p}^{\,2}+M^2c^2}}{c^2|\vec{p}\,|\sin\theta_1} \\ &= \frac{R}{c}\sqrt{\frac{1+M^2c^2/\vec{p}^{\,2}}{1-\cos^2\theta_1}} \end{aligned} \tag{1.3}$$

where R is the inner radius of the barrel;

– if the scattering angle is $18^o \leq \theta_1 \leq 32^o$ or $148^o \leq \theta_1 \leq 162^o$, using the previous argument, the anti-neutron hits one of the endcaps, longer red trace in fig. **??**, and the time-of-flight is

$$t_2 = \frac{L}{c} \frac{\sqrt{1 + M^2c^2/\vec{p}^2}}{\cos\theta_2}\,, \tag{1.4}$$

where L is the distance of the endcap from the interaction point (IP).

Using the formulae of eqs. (1.3) and (1.4) and assuming an angular uncertainty: $\delta\theta = 80$ mrad which gives errors directly on $\cos\theta_1$ and $\cos\theta_2$ we have

$$\begin{aligned}
\delta p_{\text{barrel}} &= \left(\frac{Mc^2}{R}\right)^2 \frac{t_1}{p\left[\left(\frac{t_1 c}{R}\right)^2 \sin^2\theta_1 - 1\right]^2} \left[t_1 \cos\theta_1 \delta\cos\theta_1 - \sin^2\theta_1 \delta t_1\right]\,, \\
\delta p_{\text{endcap}} &= \left(\frac{Mc^2}{L}\right)^2 \frac{-t_2\cos\theta_2}{p\left[\left(\frac{t_2 c}{R}\right)^2 \cos^2\theta_2 - 1\right]^2} \left[t_2 \delta\cos\theta_2 + \cos\theta_2 \delta t_2\right]\,.
\end{aligned} \tag{1.5}$$

2. Without π^0

10000 events $e^+e^- \to n\,\overline{n}\,\gamma_{\text{IS}}$ have been generated with the following properties

- center of mass energy ..... $E_{\text{CM}} = 3.77$ GeV;
- photon energy ..... $0.16\,\text{GeV} \leq E_\gamma \leq \frac{E_{\text{CM}}}{2}\left(1 - \frac{4M_n^2}{E_{\text{CM}}^2}\right)$;
- photon scattering angle ..... $\theta_\gamma \leq 3$ mrad.

Figure 1 shows how the $n\overline{n}$ invariant mass distribution changes as a consequence of the geometrical cut first, and then the kinematical fit (KF). The geometrical acceptance of the BESIII detector is

- $\theta \in [35^o, 145^o]$ for the barrel;
- $\theta \in [18^o, 32^o] \cup [148^o, 162^o]$ for the endcaps.

The cut corresponds to the requirement that the antineutron is produced within this acceptance. The KF instead, is performed assuming that only the initial state (IS) photon and the antineutron are detected. If we consider only the events with KF-χ^2 below 200, see fig. 2, we get the $n\overline{n}$ distribution shown as a black histogram in fig. 1. In other words, only $\sim$80% of the events which have passed the geometrical cut survives to the KF procedure.

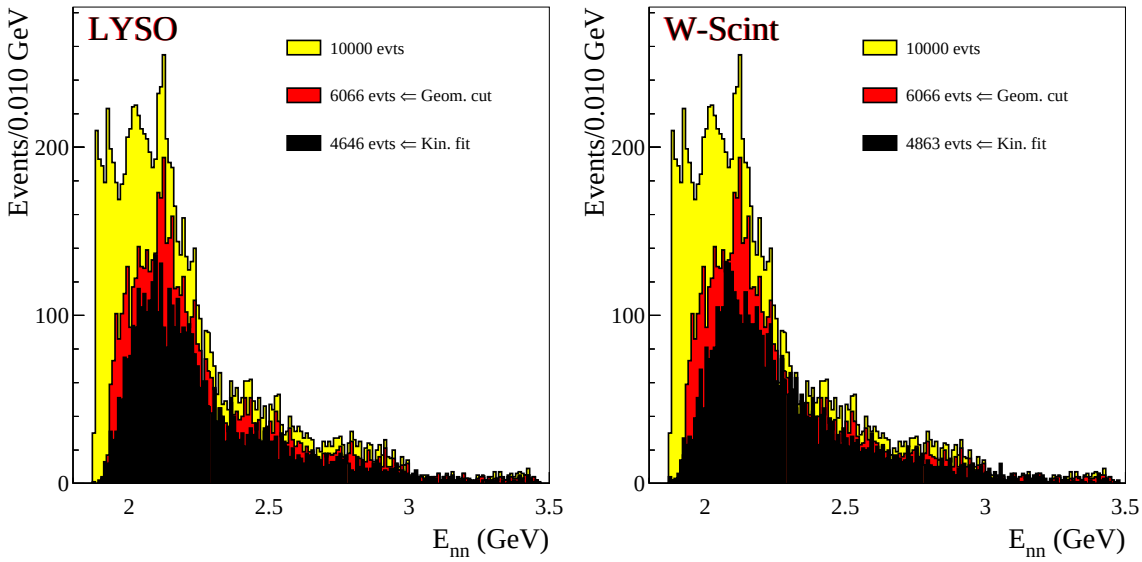

Figure 1: The yellow histogram shows the generated $n\overline{n}$ invariant mass distribution that corresponds to 10000 events. This number reduces to 6066 when the geometrical cut is applied and, finally to 4646 in case of LYSO (left) and 4863 in case of W-Scint (right) after the kinematical fit. See text for details.

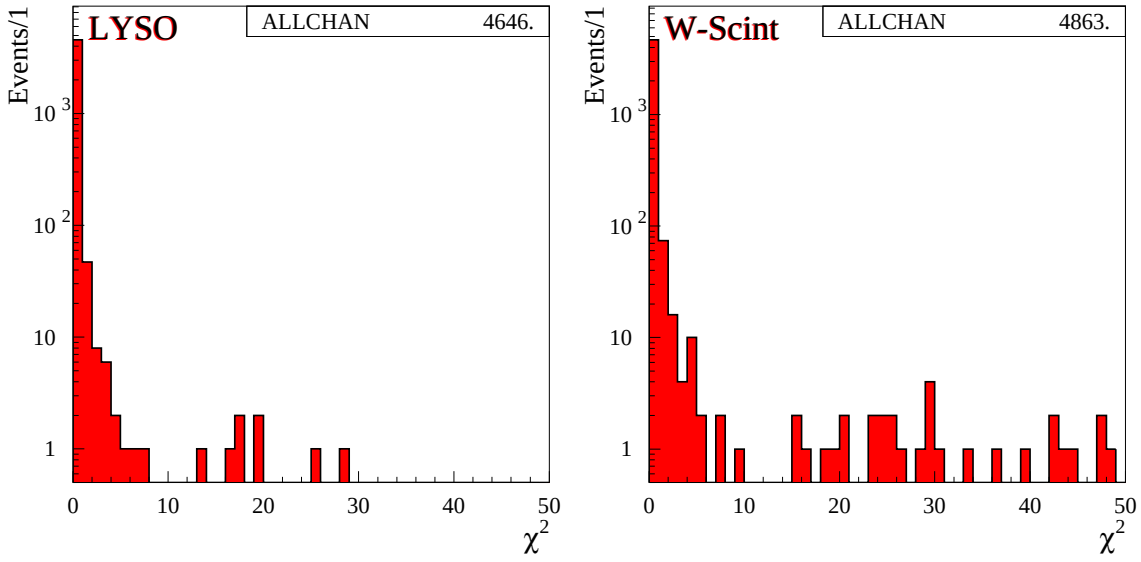

Figure 2: χ^2 distribution for $e^+e^- \to n\overline{n}\gamma_{\rm IS}$ events, where only $\gamma_{\rm IS}$ and $\overline{n}$ are detected. LYSO on the left and W-Scint on the right.

2.1 Energy slices in E_{nn}

We consider seven values of E_{nn}, from 2.0 up to 3.2 GeV in steps of 0.2 GeV. Figures 3 and 4 show the E_{nn} energies reconstructed with the KF procedure. These distributions

have been fitted with two Gaussians, i.e. the fit function is

$$f(E_{nn}) = \sum_{i=1}^{2} A_i \exp\left[\frac{(E_{nn} - E_i)^2}{2\sigma_i^2}\right] . \tag{2.1}$$

The total width is defined as

$$\sigma_{\rm tot} = \frac{\sigma_{\rm L} + \sigma_{\rm R}}{2} , \qquad \delta\sigma_{\rm tot} = \frac{|E_1 - E_2|}{2} , \tag{2.2}$$

where $\sigma_{\rm L}$ and $\sigma_{\rm R}$ satisfy the constraint

$$\int_{\overline{E}}^{\overline{E}+\sigma_{\rm R}} f(E)dE = \int_{\overline{E}-\sigma_{\rm L}}^{\overline{E}} f(E)dE = 0.341 \cdot \int_{-\infty}^{+\infty} f(E)dE . \tag{2.3}$$

In this way sigma is the mean value of the left and right intervals that contain the 34% of events starting from the center of mass of the distribution $\overline{E}$, defined as

$$\overline{E} = \frac{E_1/\sigma_1^2 + E_2/\sigma_2^2}{1/\sigma_1^2 + 1/\sigma_2^2} . \tag{2.4}$$

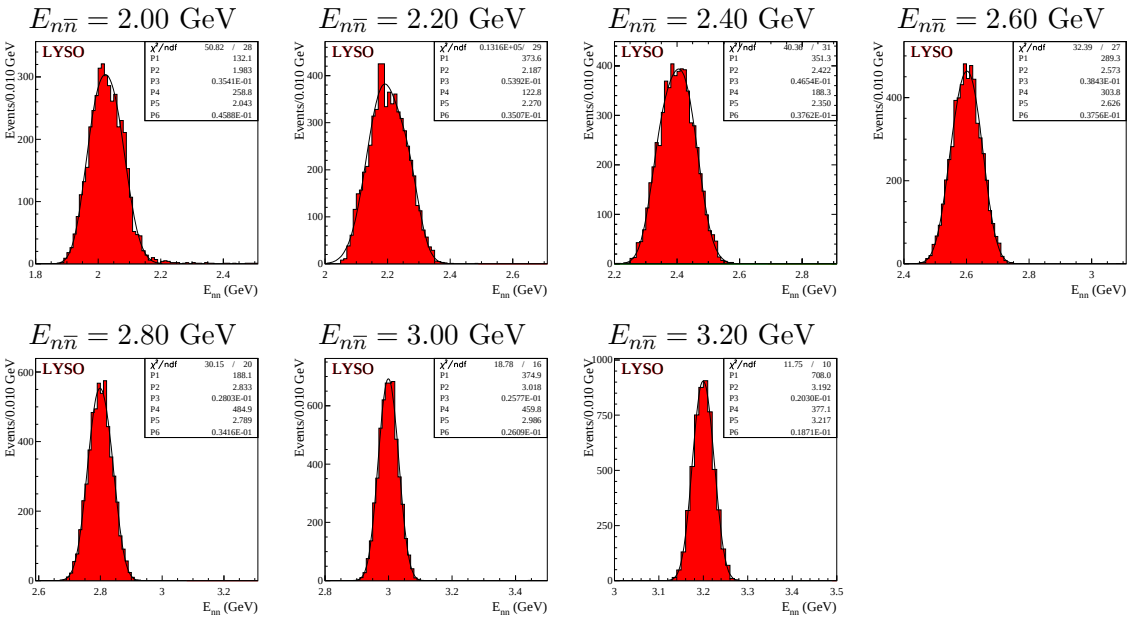

Figure 3: Energy distributions obtained in the case of LYSO detector. The curves are the fits.

The result of this computation is shown in fig. 5 in both cases, LYSO and W-Scint. Finally fig. 6 shows the percentage of events which survives to the geometrical and χ^2 cuts. More in detail the geometrical cut corresponds to require that **only** $\overline{n}$ ends up in BESIII. This means that it has to be produced with scattering angle θ_2 such that

$$\underbrace{|\cos\theta_2| \leq \cos(35^o)}_{\text{barrel}} \quad \text{or} \quad \underbrace{\cos(32^o) \leq |\cos\theta_2| \leq \cos(18^o)}_{\text{endcaps}} . \tag{2.5}$$

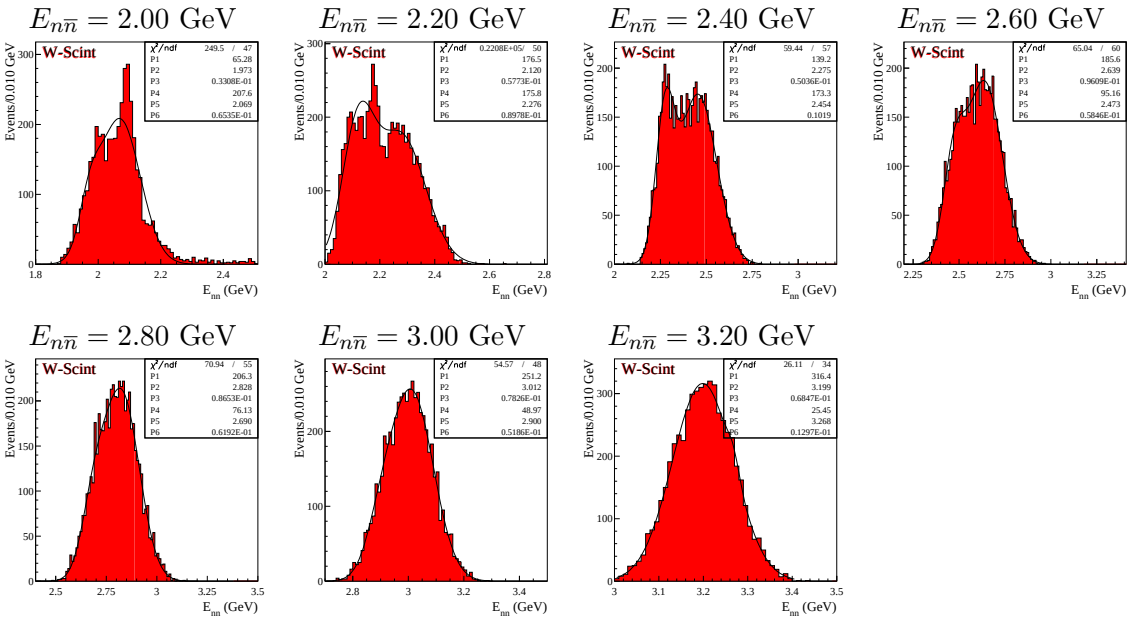

Figure 4: Energy distributions obtained in the case of W-Scint detector. The curves are the fits.

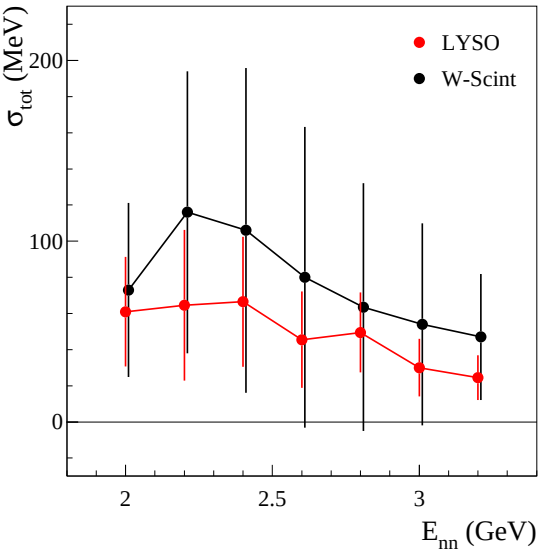

Figure 5: Energy resolution in the $n\overline{n}$ invariant mass for the LYSO (red) and W-Scint (black) case.

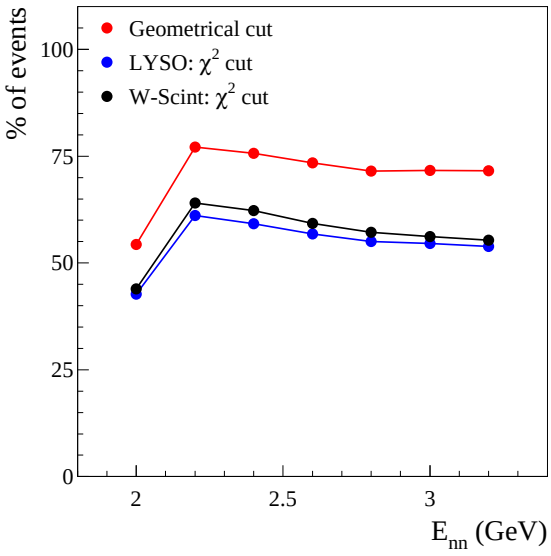

Figure 6: Percentage of events surviving to the geometrical cut, i.e. $\overline{n}$ in BESIII, and with KF-χ^2 less than 200.

The KF-χ^2 cut corresponds to

$$0 < \chi^2 < 200\,, \tag{2.6}$$

but, as can be seen in figs. 2, such a cut is widely fulfilled, almost all events are concentrated below $\chi^2 \sim 10$.

2.2 The $\overline{n}\gamma_{\rm IS}$ missing mass

Figure 7 and 8 show, in case of LYSO and W-Scint respectively, the anti-neutron-IS photon missing mass for different values of E_{nn}.

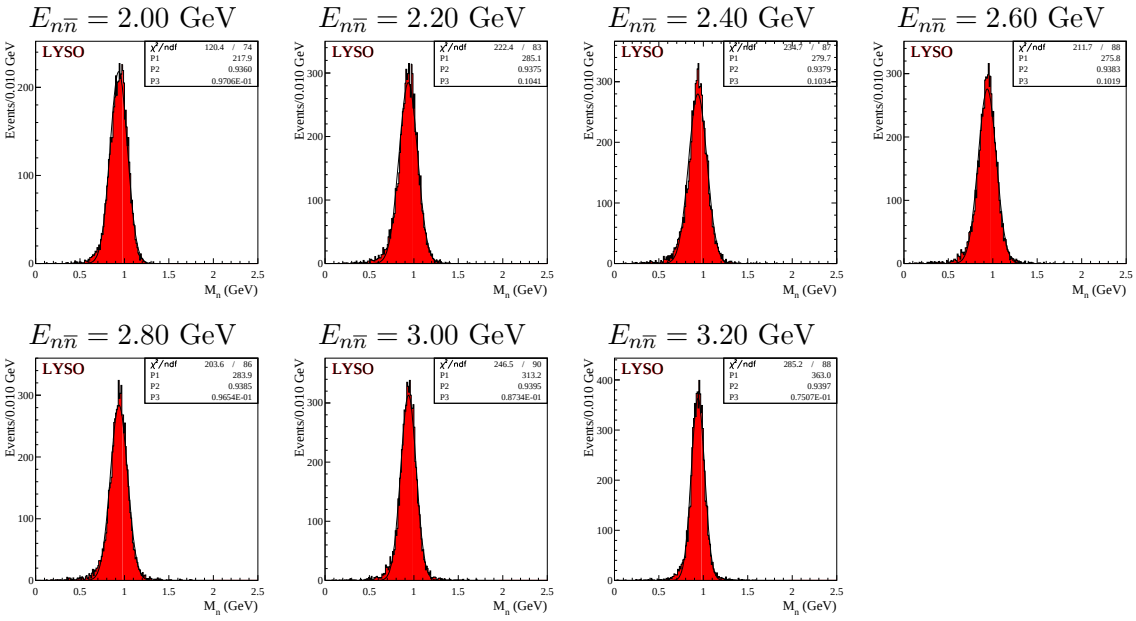

Figure 7: Anti-neutron-IS photon missing mass distributions obtained in the case of LYSO detector for seven energies. The curves are the fits.

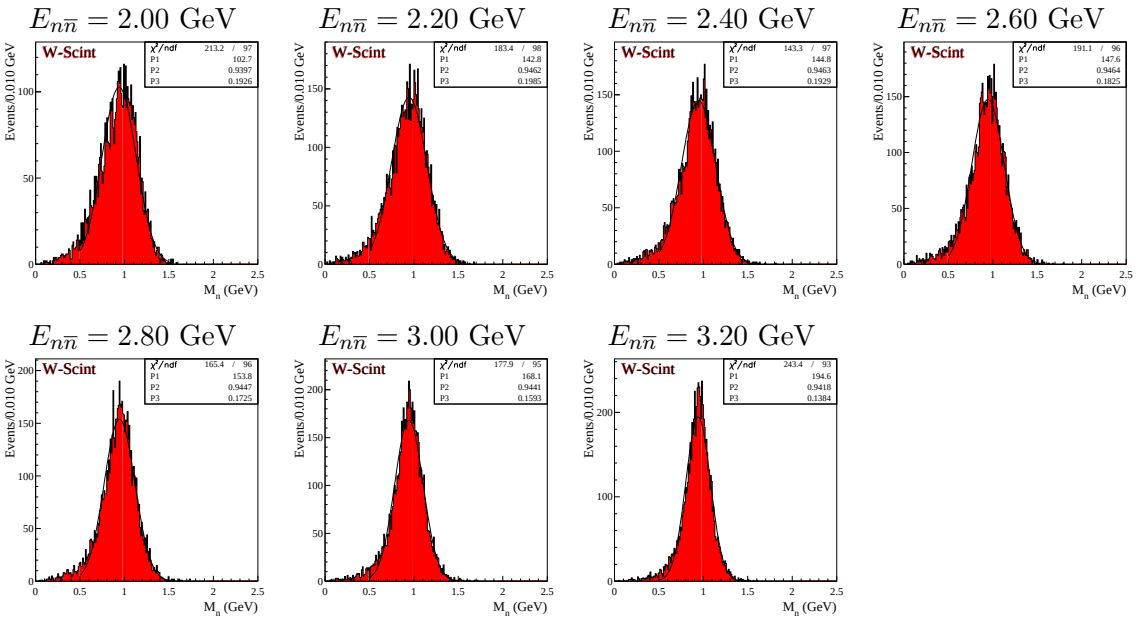

Figure 8: Anti-neutron-IS photon missing mass distributions obtained in the case of W-Scint detector for seven energies. The curves are the fits.

In fig. 9 we report trends of the n width as obtained fitting distributions of figs. 7 and 8.

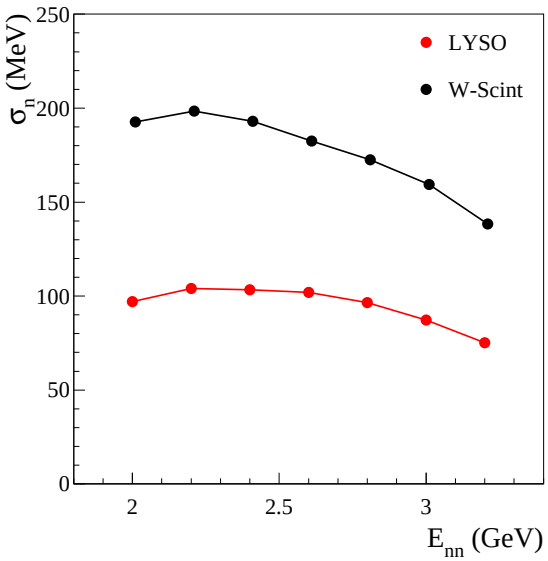

Figure 9: Widths of the $e^+e^-\gamma_{IS}\overline{n}$ missing mass distributions in case of LYSO (red) and W-Scint (black) case.

3. Including π^0

We consider now the contamination due to the production of $\gamma_{IS}n\overline{n}\pi^0$ final states, where we assume all the π^0's missed. This represents an upper limit of what we expect. The $e^+e^- \to n\overline{n}\pi^0\gamma_{IS}$ cross section has been estimated using the *BABAR* data of Ref. [1].

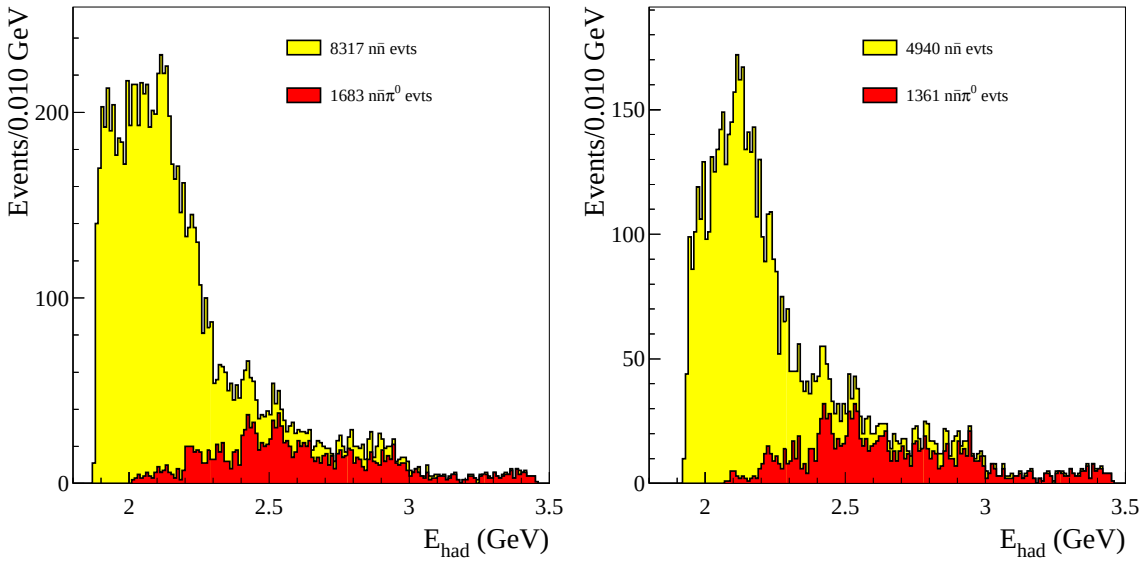

Figure 10: Yields of generated $e^+e^- \to n\overline{n}\gamma_{IS}$ events in yellow and $e^+e^- \to n\overline{n}\pi^0\gamma_{IS}$ in red before (right) and after (right) the geometrical cut.

Pictures of fig. 10 show the yields of generated events, without any cut on the left, with the geometrical cut on the right. Portions of pure $e^+e^- \to n\overline{n}\gamma_{IS}$ and $e^+e^- \to n\overline{n}\pi^0\gamma_{IS}$ are indicated by the yellow and red histograms respectively.

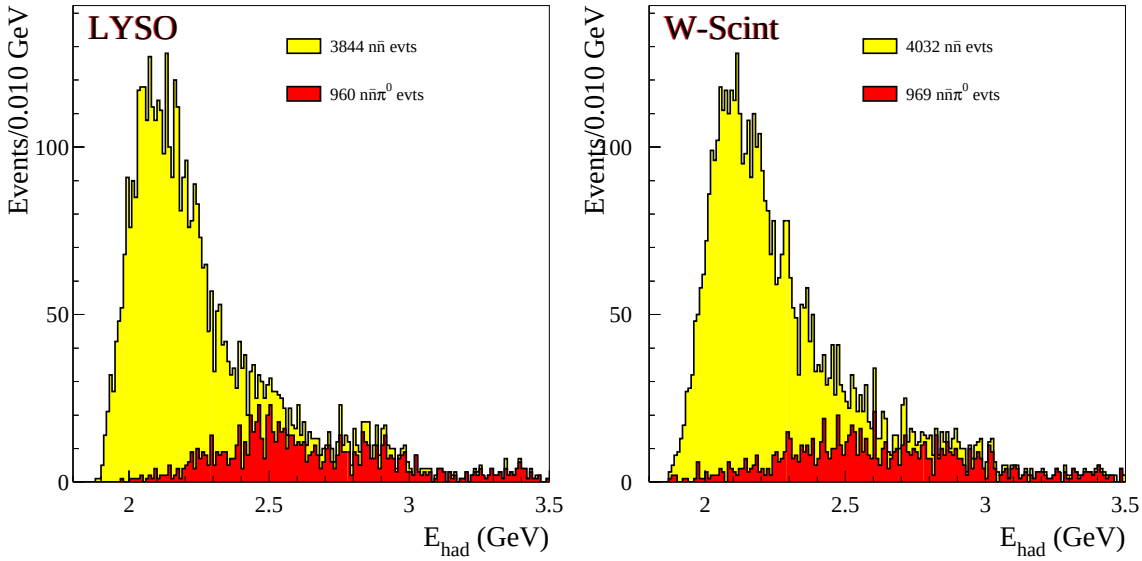

Figure 11: Yields of generated $e^+e^- \to n\overline{n}\gamma_{IS}$ events in yellow and $e^+e^- \to n\overline{n}\pi^0\gamma_{IS}$ in red before (right) and after (right) the KF.

Pictures of fig. 11 show yields after the KF in case of LYSO and W-Scint detectors. The amount of π^0 contamination remains almost unchanged. Figure 12 shows the two χ^2's.

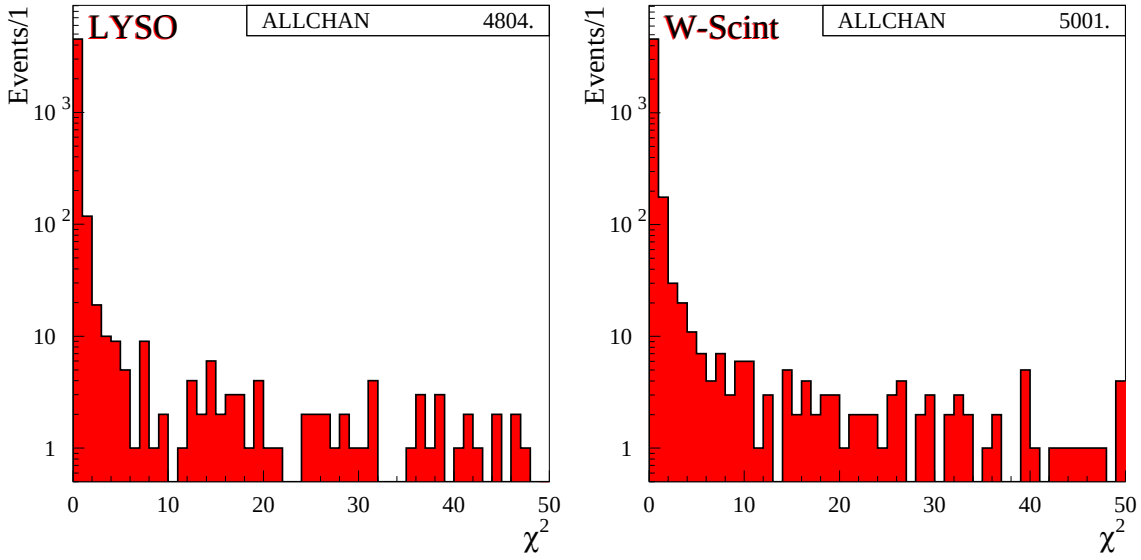

Figure 12: χ^2 distribution for $e^+e^- \to n\overline{n}\pi^0\gamma_{IS}$ events, where only γ_{IS} and $\overline{n}$ are detected. LYSO on the left and W-Scint on the right.

3.1 Energy slices in $E_{\rm had}$

As before, we consider seven values of $E_{\rm had}$, the energy of the whole hadronic final state, from 2.0 up to 3.2 GeV in steps of 0.2 GeV. Figures 13 and 14 show the $E_{\rm had}$ energies reconstructed with the KF procedure, in red the pure $n\overline{n}\gamma_{\rm IS}$ final states, in green $n\overline{n}\pi^0\gamma_{\rm IS}$. These distributions have been fitted with two Gaussians.

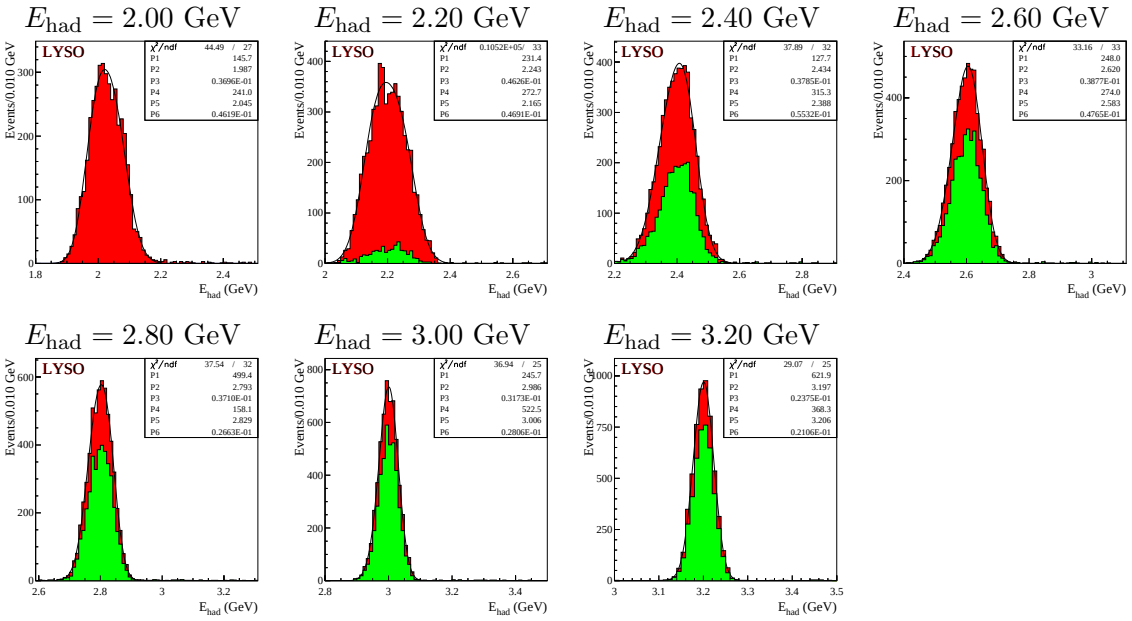

Figure 13: Energy distributions obtained in the case of LYSO detector. Red and green histograms identify pure $n\overline{n}\gamma_{\rm IS}$ and $n\overline{n}\pi^0\gamma_{\rm IS}$ contributions respectively. Black curves are the fits.

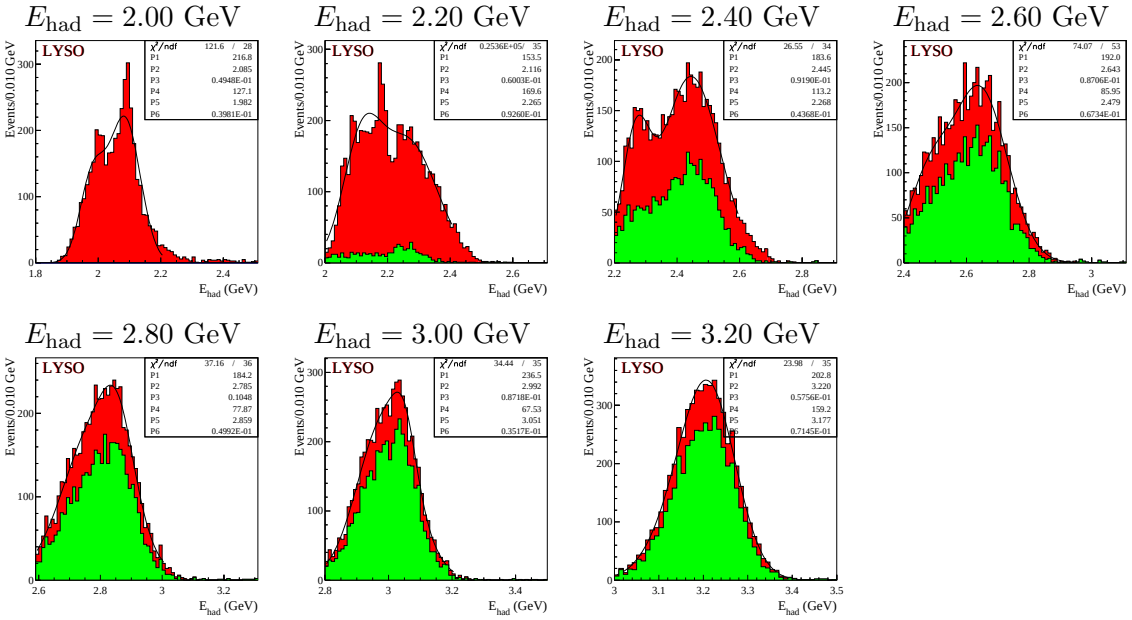

Figure 14: Energy distributions obtained in the case of W-Scint detector. Red and green histograms identify pure $n\overline{n}\gamma_{\rm IS}$ and $n\overline{n}\pi^0\gamma_{\rm IS}$ contributions respectively. Black curves are the fits.

Figures 15 and 16 show the resolutions computed as in Sec. 2.1, and the percentage of events surviving to the geometrical and KF cuts.

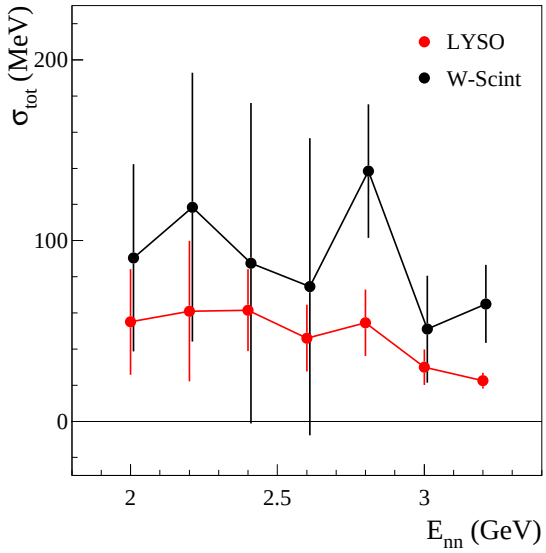

Figure 15: Energy resolution in the hadronic invariant mass for the LYSO (red) and W-Scint (black) case.

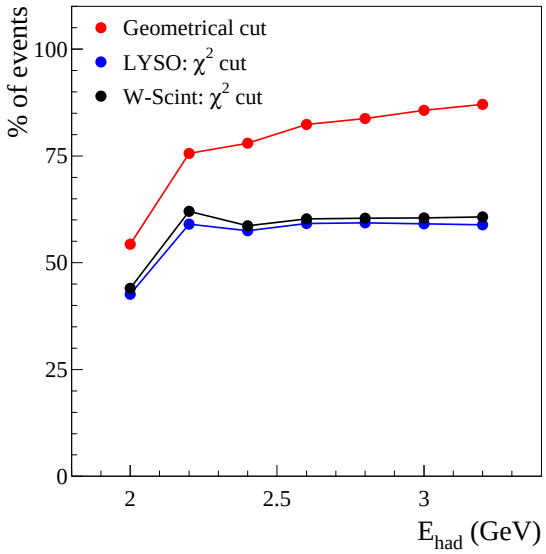

Figure 16: Percentage of events surviving to the geometrical cut, i.e. $\overline{n}$ in BESIII, and with KF-χ^2 less than 200.

These events, as it is shown in previous distributions and in detail in fig. 17, are not pure $n\overline{n}$ but contain also an $n\overline{n}\pi^0$ contamination, which survives to the KF procedure.

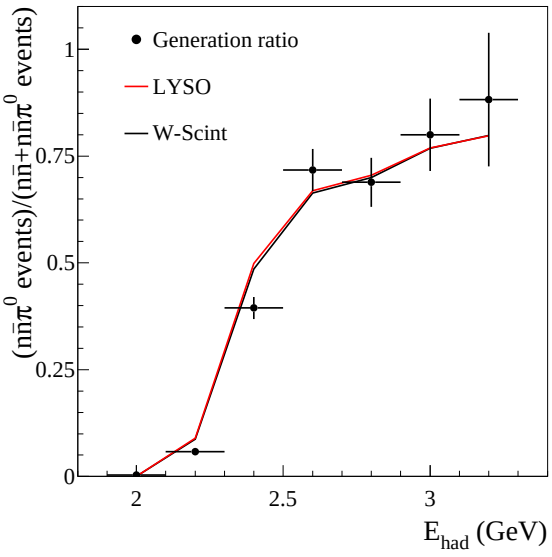

Figure 17: Fraction of $n\overline{n}\pi^0$ after the KF procedure for LYSO (red) and W-Scint (black), in comparison with the generation ratio (points).

3.2 The $\overline{n}\gamma_{\rm IS}$ missing mass with π^0 contamination

Figure 18 and 19 show, in case of LYSO and W-Scint respectively, the anti-neutron-IS photon missing mass for different values of $E_{\rm had}$.

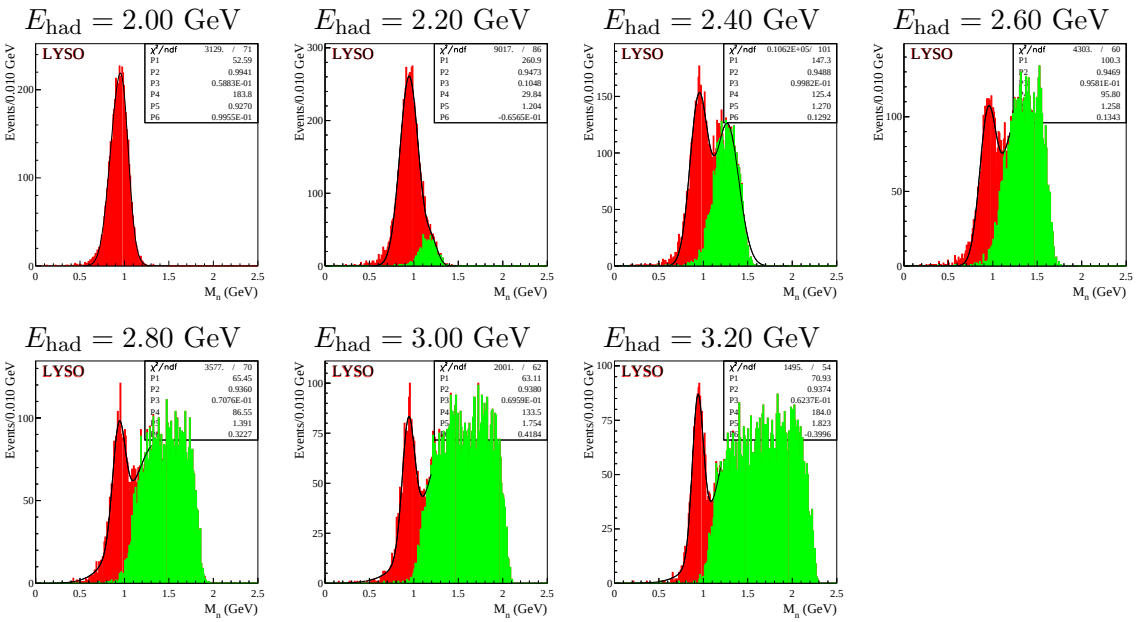

Figure 18: Anti-neutron-IS photon missing mass distributions obtained in the case of LYSO detector for seven energies. Red and green histograms stand for pure $n\overline{n}$ and $n\overline{n}\pi^0$ contributions. The curves are the fits.

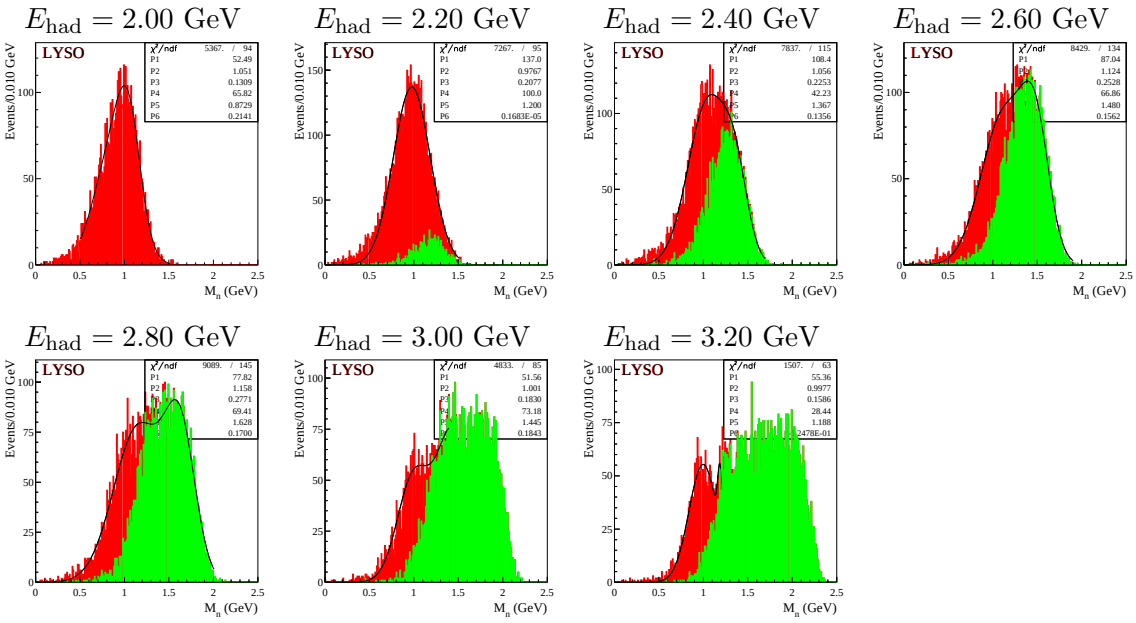

Figure 19: Anti-neutron-IS photon missing mass distributions obtained in the case of W-Scint detector for seven energies. Red and green histograms stand for pure $n\overline{n}$ and $n\overline{n}\pi^0$ contributions. The curves are the fits.

In fig. 20 we report trends of the n width as obtained fitting distributions of figs. 18 and 19 with two Gaussians and taking the widths of the only one centered around the neutron mass (red histograms).

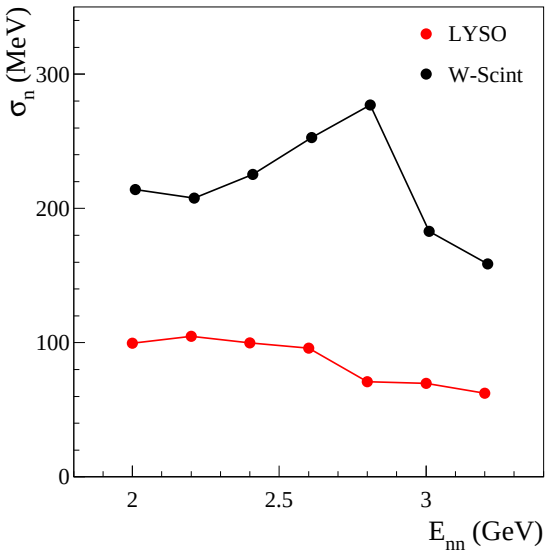

Figure 20: Widths of the $e^+e^-\gamma_{\rm IS}\overline{n}$ missing mass distributions in case of LYSO (red) and W-Scint (black) case.

References

[1] B. Aubert *et al.* [*BABAR* Collaboration], Phys. Rev. D **73**, 012005 (2006) [arXiv:hep-ex/0512023].